Provided for non-commercial research and education use.
Not for reproduction, distribution or commercial use.

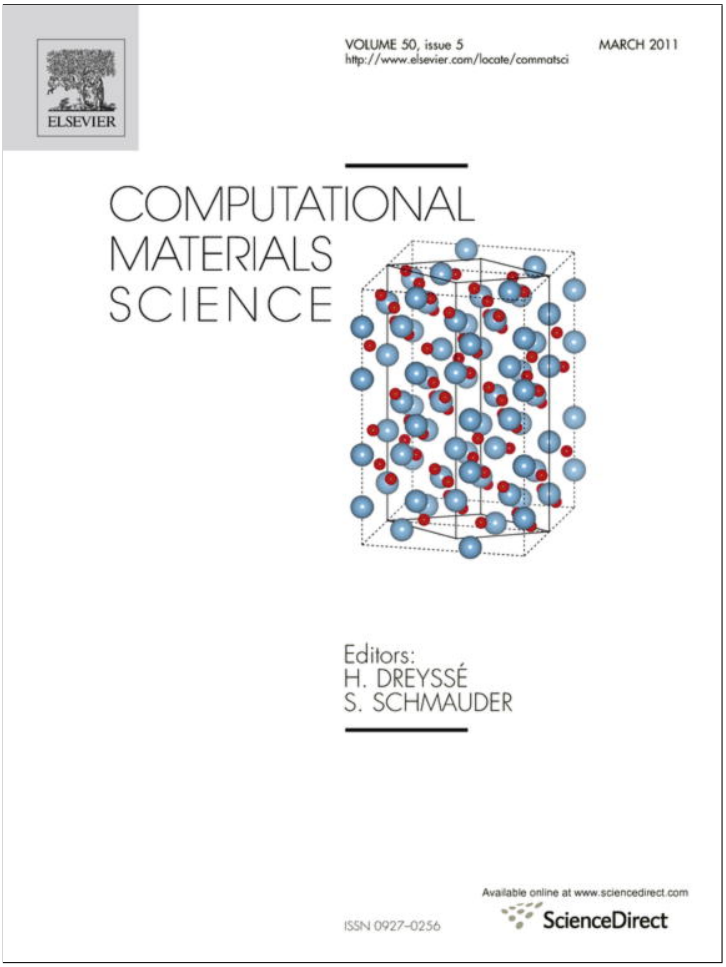

This article appeared in a journal published by Elsevier. The attached copy is furnished to the author for internal non-commercial research and education use, including for instruction at the authors institution and sharing with colleagues.

Other uses, including reproduction and distribution, or selling or licensing copies, or posting to personal, institutional or third party websites are prohibited.

In most cases authors are permitted to post their version of the article (e.g. in Word or Tex form) to their personal website or institutional repository. Authors requiring further information regarding Elsevier's archiving and manuscript policies are encouraged to visit:

http://www.elsevier.com/copyright

Author's personal copy

Computational Materials Science 50 (2011) 1651–1660

Contents lists available at ScienceDirect

Computational Materials Science

journal homepage: www.elsevier.com/locate/commatsci

Phase transformations, dislocations and hardening behavior in uniaxially compressed silicon nanospheres

L.M. Hale [a,*], X. Zhou [b], J.A. Zimmerman [b], N.R. Moody [c], R. Ballarini [d], W.W. Gerberich [a]

[a] Department of Materials Science, University of Minnesota, Minneapolis, MN 55455, USA
[b] Department of Mechanics of Materials, Sandia National Laboratories, Livermore, CA 94550, USA
[c] Department of Hydrogen and Metallurgy Science, Sandia National Laboratories, CA 94550, USA
[d] Department of Civil Engineering, University of Minnesota, Minneapolis, MN 55455, USA

ARTICLE INFO

Article history:
Received 4 November 2010
Received in revised form 15 December 2010
Accepted 16 December 2010
Available online 1 February 2011

Keywords:
Phase transformations
Dislocations
Nanostructure
Molecular dynamics
Silicon

ABSTRACT

Molecular dynamics has been used to simulate the uniaxial compression of single crystal silicon nanospheres using the Tersoff potential. The resulting yield behavior is shown to vary with changes in temperature, sphere size, and crystallographic orientation with respect to the loading direction. Only compression along the [1 0 0] crystallographic direction resulted in the formation of the β-Sn phase. A temperature dependent hardening response is observed in all orientations independent of the β-Sn phase transformation. Dislocation activity is detected at elevated temperatures in the largest sphere indicating a critical temperature and size for nucleation. Consequences of these dislocations to simulating strength properties at the nanoscale are discussed.

© 2011 Elsevier B.V. All rights reserved.

1. Introduction

Much work has been done examining material behaviors at the nano-scale due to their differences from bulk properties. In particular, spherical silicon nanoparticles were shown by Gerberich et al. [1] to be harder than bulk silicon under compression. The work proposed that the hardening was the result of dislocation loops forming in the spheres at the contact points. The experimental evidence supported this by showing displacement excursions occurring in the load vs. displacement curves indicative of dislocation formation. That paper also contains the first attempt to simulate the behavior of the spheres in compression using molecular dynamics and the MEAM potential. However, only amorphous damage was observed at the contact points most likely due to the low simulated temperature, the high displacement rate, and perhaps the small sphere size of 12 nm in diameter.

In 2007, Valentini et al. [2] performed simulations of Si sphere compression along the [1 0 0] crystalline direction using the Tersoff potential at 0 K. The center of the spheres was shown to undergo a transformation from the diamond cubic (DC) crystal structure to the β-Sn structure. Measurements of the applied load and resulting contact stresses during the compression showed extensive hardening of the spheres, which was attributed to the phase transformation. Repeated loading allowed the plastic behavior to accumulate resulting in the majority of the sphere transforming to β-Sn. Annealing of the deformed spheres at an elevated temperature allowed for a reverse phase change to occur and the spheres returned close to their original shape.

For the present work, the Tersoff potential was used to further study the deformation behavior of silicon nanospheres. The Tersoff potential was originally developed to match the thermodynamic properties of silicon in all of its known solid phases [3]. As such, it gives the correct cohesive energies for the different phases along with the conditions that favor each phase making it ideal for studying the relationship between phase transformations and hardening behavior.

By examining the effects of varying the compression orientation and simulation temperature, a wide range of yielding behaviors was observed. In particular, the formation of the β-Sn phase was shown to be highly dependent on the crystallographic orientation of the compressive loading. Large hardness values were also observed, but were shown to be independent of the amount of β-Sn present within the spheres. An alternative explanation for these high hardness values observed during simulations using the Tersoff potential is proposed. The simulation results are compared to the previous experimental results providing a useful direction for further work.

* Corresponding author. Address: 421 Washington Ave. SE, Minneapolis, MN 55455-0132, USA. Tel.: +1 612 624 0515; fax: +1 612 626 7246.
E-mail address: halex082@umn.edu (L.M. Hale).

0927-0256/$ - see front matter © 2011 Elsevier B.V. All rights reserved.
doi:10.1016/j.commatsci.2010.12.023

Author's personal copy

2. Computational procedure

All work was done using the LAMMPS molecular dynamics simulation code [4] with a timestep of 0.001 ps. Three sphere sizes were used with 5, 10 and 20 nm diameters (3265, 26,167, and 2,09,121 atoms respectively). Using a Nose–Hoover thermostat [5], the 5 nm sphere was analyzed at 0, 300 and 600 K, while the 10 nm and 20 nm spheres were studied at 0 and 300 K. All spheres were compressed along the [1 0 0] crystal direction. During separate simulations the 5 and 10 nm spheres were also compressed along [1 1 0] and [1 1 1] directions. The particular version of the Tersoff potential used here is the third of the originally published parameters [6], which were chosen to give the best fit to the elastic properties of the diamond cubic phase. For these reasons, this potential is widely used for MD simulations of mechanically deformed silicon.

Initial sphere creation was done by generating all of the perfect bulk crystal lattice positions within a geometrically defined sphere. Following this, the sphere was annealed at 400 K for 1000 ps to relax the surface atoms before quenching down to 0 K.

Two planar indentation potentials were used to compress the spheres, one placed above the sphere (related to the direction of the y-axis) and the other equidistant below. This potential applies a force onto atoms according to their coordinates as given by

$$F_y(y) = ck(y - y_i)^2 \tag{1}$$

where F_y is the force in the y direction that the indenter applies onto each atom, k is a constant (taken to be 10.0 eV/Å), y is the y-coordinate for that atom, and y_i is the y-coordinate of the indenter. To insure that both indenters apply a repulsive force when they contact the sphere, for the upper indenter $c = -1$ when $y \geqslant y_i$ and $c = 0$ when $y < y_i$, whereas for the lower indenter $c = 1$ when $y \leqslant y_i$ and $c = 0$ when $y > y_i$. The total applied load of the indenter, P, can be easily calculated by summing all of the forces it applies onto the atoms of the sphere: $P = \sum F_y$.

In comparison to using a rigid plane of atoms for the indenter, the planar potential is computationally more efficient by reducing the total number of atoms in the system and allows for the applied load and the contacted atoms to be easily identified. However, the indenter potential lacks the slight attraction just before contact and the atomic roughness associated with a plane of atoms. This roughness and attraction are both small in scale relative to the total displacements and the resulting loads that their effects are negligible except at the initial contact/detachment of the indenters with the sphere.

Both indenters utilized inward velocities of 0.003125 Å/ps = 0.3125 m/s, resulting in a total displacement rate that is double this value. The indenters were allowed to compress the spheres until an engineering compressive strain (total displacement/diameter) between 0.4 and 0.6 before the spheres were unloaded at the same rate. During compression, the linear and rotational momenta of the total sphere were subtracted from each atom to prevent the sphere from rotating and drifting before and during compression.

Phase identification was aided using a parameter related to the angles between the bonds of all of the nearest neighbors. This "angular" parameter was taken to be

$$\frac{1}{N_b}\sum_{j=1}^{N}\sum_{k=j+1}^{N}\left(\cos\theta_{ijk} - \cos\theta_{\mathrm{DC}}\right)^2 \tag{2}$$

where N is the number of nearest neighbors that atom i has, θ_{ijk} is the angle between atoms i, j, and k, θ_{DC} is the bond angle for bulk diamond cubic, and N_b is the number of bond angles that have been summed over. In essence, the difference in the cosine of the bond angle with respect to the perfect diamond cubic structure is squared, and then averaged for all bond pairs around a given atom. For the results presented here, a cutoff of 3 Å was used to determine the nearest neighbors included in this expression. This angular parameter is dependent on each atom's coordination number, but is advantageous as it can distinguish between multiple phases and defects that have the same coordination number. The parameter's formulation is related to the three-body term of the Stillinger–Weber potential [7].

Dislocation activity was monitored primarily with the slip vector parameter [8], given by

$$\vec{S}_i = -\frac{1}{N_s}\sum_{j\neq i}^{N}\left(\vec{R}_{i,j} - \vec{R}^0_{i,j}\right) \tag{3}$$

where N is the total number of nearest neighbors to atom i, N_s is the number of neighbors that are on an adjacent slip plane to atom i (e.g., $N_s = 1$ if slip occurs on an {1 1 1} diamond cubic lattice), $\vec{R}^0_{i,j}$ is the vector from atom i to its neighbor j at an initial unstrained reference configuration, and $\vec{R}_{i,j}$ is the corresponding vector at the current configuration. By finding the relative displacement of the nearest neighbor atoms j with respect to a given atom i, it can be determined if a plane neighboring atom i has slipped and in what direction. Dividing by $-N_s$ scales the vector's magnitude so that it will be equal to the Burgers vector of the dislocation that caused the slip.

3. Results and discussion

The load vs. displacement curves obtained from the 10 nm diameter spheres are shown in Fig. 1. Similar compression behavior is observed in the 5 and 20 nm diameter spheres, which are not shown. For a given orientation, the load at small displacements is nearly identical at the different measuring temperatures corresponding to the spheres behaving elastically. Following this, the higher temperature runs deviate from the 0 K curve (e.g., for the 10 nm spheres the 300 K load is less than the 0 K load for displacements greater than 1–2 nm.) This indicates that yielding has occurred in the higher temperature runs resulting in a substantial change in the loading rate. For the 0 K curves, the [1 0 0] compression shows a similar drop in slope indicating yielding followed by a sharp peak in the applied load at high displacements, whereas the [1 1 0] and [1 1 1] compressions continue to increase fairly steadily throughout the loading with the occasional drop indicating some form of yielding. These two behaviors result in the maximum load at 0 K being approximately 2 times greater than the maximum loads at the higher temperatures for all three orientations.

The radius of the contact area, a, between the spheres and the plates was calculated by identifying the atoms (N_a) that were within 0.1 Å from each of the indenters. By identifying the center of mass ($X_{C.M.}$ and $Z_{C.M.}$) for that collection of atoms, the contact radius was found with a formula given by Vergeles et al. [9]

$$a^2 = \frac{2}{N_a}\sum_{i=1}^{N_a}\left[(x_i - X_{C.M.})^2 + (z_i - Z_{C.M.})^2\right] \tag{4}$$

This measured contact radius is shown in Fig. 2a for the 20 nm sphere and Fig. 2b for the 10 nm spheres at 0 K. Along with measured contact radius squared are the predicted values for both the elastic Hertzian model [10] and the Geometric intersection between a sphere and a plane that are calculated from the displacement, δ, and sphere radius, R

$$a^2 = \frac{1}{2}R\delta \quad \text{Hertz;} \tag{5}$$

$$a^2 = R\delta - \frac{\delta^2}{4} \quad \text{Geometric.} \tag{6}$$

These two models are examined here as they are heavily used with the experimental results in estimating the contact radius, as

Author's personal copy

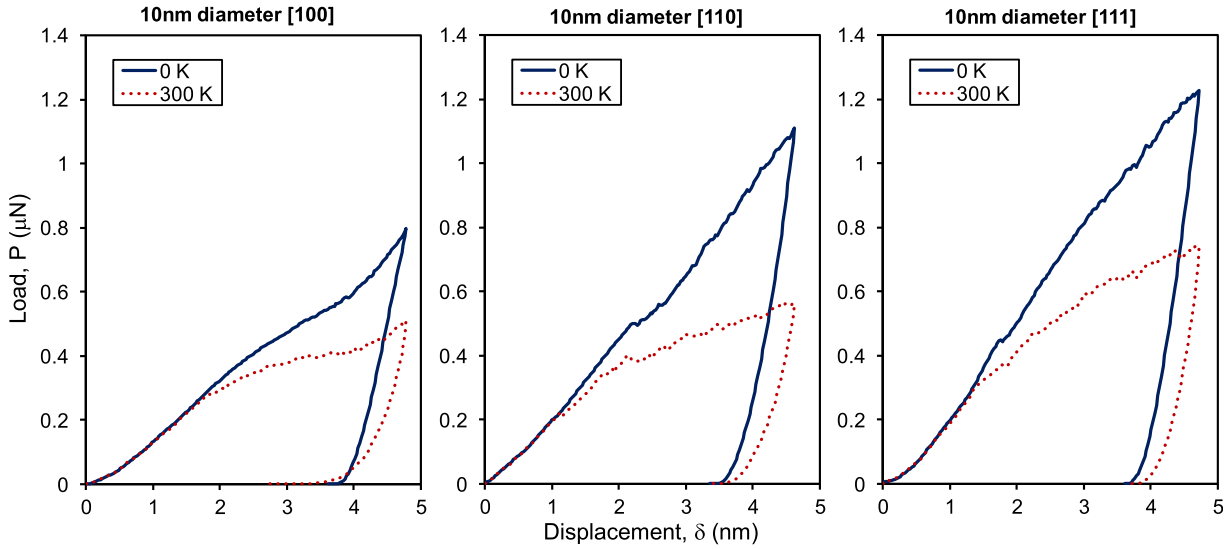

Fig. 1. The load vs. displacement curves for all 10 nm simulations. Note that the maximum force is nearly twice as high for the 0 K simulations than it is for the other higher temperature simulations.

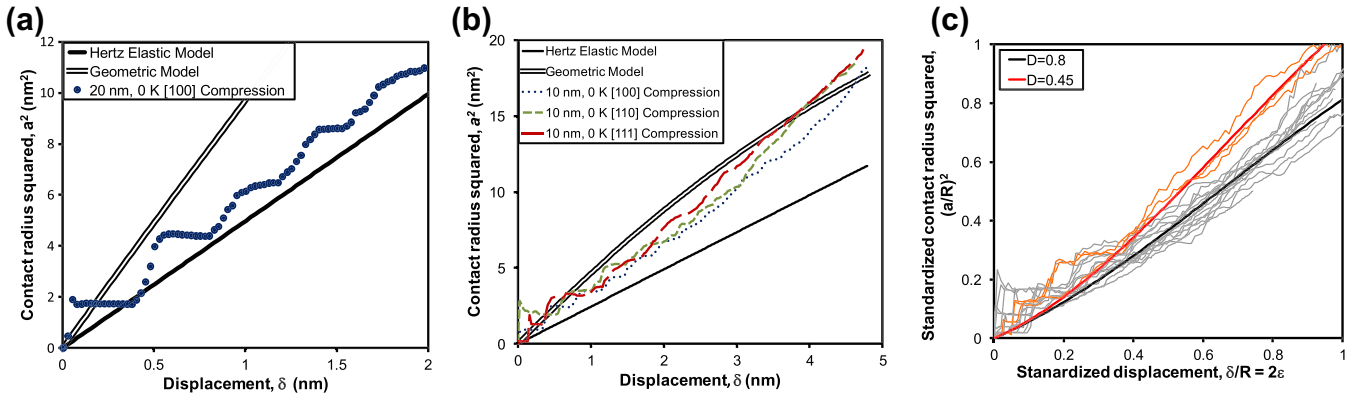

Fig. 2. The squared contact radius vs. displacement. (a) At low displacements for the 20 nm diameter spheres (0 K shown), the contact area jumps due to the surface steps resulting in discontinuous behavior, but still loosely follows the Hertz model. (b) As seen with the 10 nm diameter data at 0 K, at moderate displacements, the curves fall directly between the elastic and the Geometric models. At high displacements, the contact area begins to increase at a higher rate deviating from both models. The high displacement deviation is more profound for the 300 K compressions (not shown here). (c) The contact radius squared for all of the data shown with the new model fit from Eq. (7).

direct measurements of this value are difficult to obtain with particles of this size. As the formulation in Eq. (4) allows for a direct measurement of the contact areas during these simulations, it offers an opportunity to study the accuracy of the two models.

Initially, at low loads the contact radius shows a discrete nature as its value stays constant for a number of steps before jumping to a larger value. See Fig. 2a. This appears to be nothing but a geometrical artifact of the sphere design and indenter potential used. The top and bottom-most atomic planes of the spheres consist of only a handful of atoms resulting in the initial contact area being relatively small. On continued loading, the outermost atomic layers are pushed far enough into the sphere that the indenters then come into contact with the next inward planes of atoms. When this occurs, the contact area suddenly increases. The effects of this jump in contact area decreases with increasing sphere size and displacement.

Fig. 2a shows that for the 20 nm diameter sphere at small displacements, the contact radius behavior still contains the discontinuous jumps, but is smooth enough to show a general trend following the Hertzian model. This is the expected behavior as only elastic behavior is seen within the sphere during this period. At moderate displacements (~1–3.5 nm for the 10 nm spheres in Fig. 2b), the measured values for all three orientations lie between the Hertzian and Geometric values, with the change in contact radius with displacement closer to the Geometric model. While neither model gives a "best fit" to the measured contact radius, they can be seen to offer an upper and lower bound during this displacement range. The largest displacements (Fig. 2b) reveal that the spheres no longer follow either model as the contact area begins to increase at a greater rate than either model predicts due to neither model accounting for expansion of the sphere in the uncompressed directions.

From these comparisons, it is possible to develop a more accurate, but yet still simple model for the contact area behavior. One method would be to linearly mix the two theoretical models. This results in an expression such as

$$a^2 = \frac{(D-\delta)a^2_{\text{Hertz}}}{D} + \frac{\delta a^2_{\text{Geo}}}{D} = \frac{1}{2}R\delta + \frac{R\delta^2}{2D} - \frac{\delta^3}{4D} \tag{7}$$

where D is a fitting constant with units of distance. This equation is a third-order polynomial fit containing only one unknown that given the appropriate choice of D fits the previously mentioned

Author's personal copy

behavior of the measured contact area for all displacements observed here.

Conceptually, at first glance Eq. (7) appears to increase the relative amount of plastic to elastic behavior as the displacement increases. However, as neither of the base models accounts for the sphere's incompressibility at large displacements, this conceptual argument is faulty. This new model gives an empirical fit to the data even though it is derived from the two mathematical models.

As seen in Fig. 2c, there is considerable variation in the values measured for the contact area under the different conditions studied here. However, comparing Eq. (7) to the measured values reveals that a D value of 0.8 R offers a decent fit to nearly all of the data. The only clear exceptions are the [1 1 1] compressions at elevated temperatures, which favor a D value closer to 0.45 R. As the constant D is fitted to the entire strain range, this variation due to the loading direction could depend on either changes in the plastic behavior or anisotropy in the elastic constants and crystal structure. With either value of D, the general trend given by Eq. (7) better predicts the measured contact area than either the Hertzian or Geometric models for the full displacement range between $0 \leqslant \delta \leqslant R$.

The averaged contact stress ($P/\pi a^2$) was also calculated for all of the samples and is shown in Fig. 3 for the 10 nm spheres plotted vs. compressive strain of the sphere ($\delta/2R$). The general behavior of the contact stress on increasing strain was that one large peak or a series of smaller peaks would initially appear at low strains corresponding to the jumps in the radius of the contact area mentioned above. After these peaks, the stress values would drop before beginning to linearly increase again indicating that the material is still behaving elastically. Between strains of 0.1 and 0.2, the behaviors of the 0 K and higher temperature simulations are seen to deviate from each other. The contact stress in the 0 K runs plateaus and remains close to the maximum value reached, while the 300 and 600 K runs have stresses that reach a maximum value before steadily decreasing with additional strain indicating a softening behavior.

The hardness values reported from the experimental results [1] were taken to be the maximum load for a given compression divided by the calculated contact area. This definition is identical to that of the averaged contact stress here allowing the two values to be compared directly. Experimentally, for a single load-unload, the hardness for bulk silicon is around 12 GPa while the reported hardness values for spheres varying between 19 and 46 nm in radius and unknown orientations were 10–40 GPa [1]. Repeated loading showed an increase in hardness suggesting that the spheres become harder as the load increases, or as the plastic damage increases.

The maximum stress values measured from these simulations do not vary by much between the temperatures: 16–24 GPa for the 0 K compressions vs. 14–22 GPa for the 300 and 600 K compressions. However, the contact stress values at the maximum strain are quite different, with 14–20 GPa at 0 K compared to 7–9 GPa at 300 K. This matches with the difference in the load vs. displacement curves in Fig. 1, where the maximum load at 0 K is approximately twice what it is at 300 K.

The maximum contact stress values from the simulations are a decent match to the experimental hardness values, with values ranging from the bulk silicon value to roughly 2 times the bulk value. A discrepancy is seen, however, in that from the experiments, the hardness increases slightly as the load increases, whereas the 300 K simulations show a marked decrease in the contact stress upon increased displacement. *This indicates that the simulations presented here using the Tersoff potential at ambient temperatures fail to give the appropriate hardening response.*

The stiffness was also calculated for the 10 nm diameter spheres at the maximum displacement by evaluating the initial slope of the unloading curves from the stress vs. strain plots. At 0 K, the values for unloading modulus for the [1 0 0], [1 1 0] and [1 1 1] directions respectively were 154, 236, and 252 GPa, while at 300 K were 103, 117 and 144 GPa. These show that the simulations performed at 0 K were 50%–100% stiffer at their maximum loadings than the similar runs at 300 K.

3.1. Phase transformations

The β-Sn phase is the first of the high pressure phases that silicon is known to form during hydrostatic compression [11,12]. The BCT5 phase is not as well known or studied, and was first proposed by Boyer et al. in 1991 [13]. Initially identified using a Stillinger–Weber potential and first principle calculations, BCT5 is a body-centered-tetragonal structure where every atom has a coordination number of 5. The presence of BCT5 has been observed in indentation simulations using a Tersoff potential [14–18], but has not yet been observed experimentally. Believed to be a metastable state, the likelihood of BCT5 actually forming is still unknown. The unit cells of the BCT5 and β-Sn silicon structures are shown in Fig. 4.

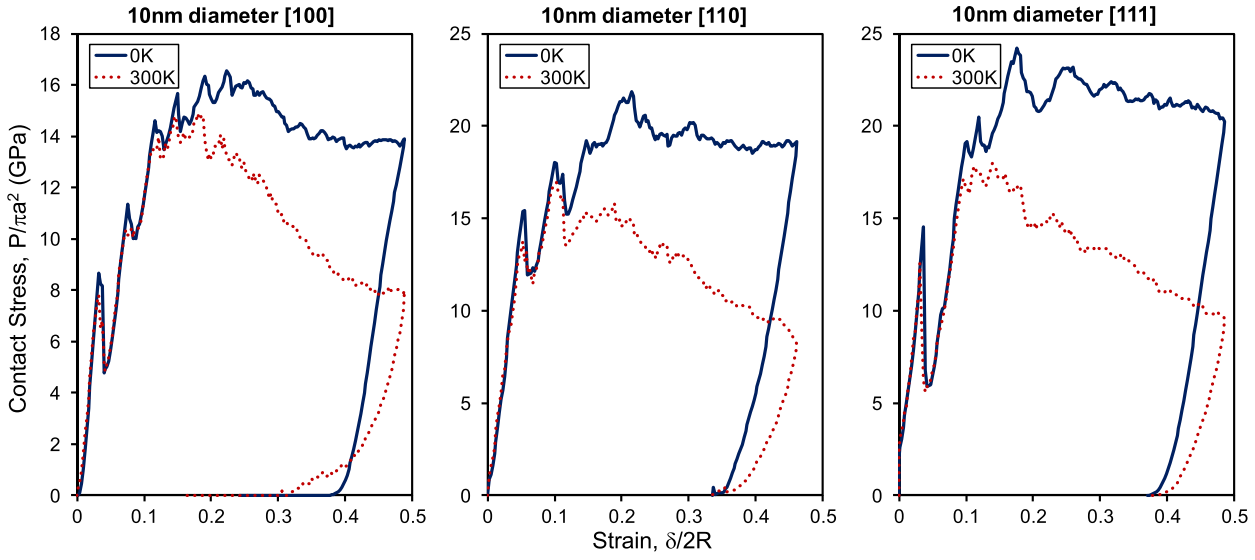

Fig. 3. The contact stress vs. engineering strain curves of the 10 nm diameter simulations.

Author's personal copy

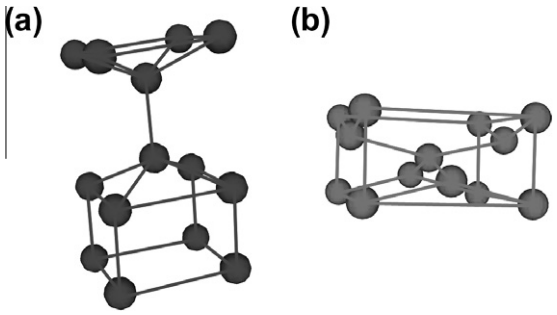

Fig. 4. Unit cells of (a) BCT5 and (b) β-Sn showing their atomic arrangements.

The lattice and elastic constants for DC, BCT5 and β-Sn were calculated near 0 K and are included in Tables 1–3 respectively. In regards to BCT5, the energy and structure is seen to be slightly closer to the first principle calculations with the Tersoff potential than with the Stillinger–Weber potential. Using the Tersoff potential also produces a very good agreement for the structure of β-Sn. In addition, it has been previously shown that the Tersoff potential correctly predicts the pressure and resulting volume changes associated with the transition from DC to β-Sn [19].

A study of the ideal positioning of the atoms in different silicon phases allowed for a determination of appropriate values of the angular parameter for each phase. From this, diamond cubic, BCT5 and β-Sn have angular values of 0, 0.12 and 0.18 respectively.

Table 1
The lattice parameter and elastic constants for the diamond cubic structure of silicon.

	Tersoff [19]	Tersoff (this work)	Experimental [19]
a (Å)	5.432	5.432	5.429
E (eV/atom)	−4.6297	−4.63	−4.63
C11 (GPa)	142.5	139.7	167
C12 (GPa)	75.4	74.1	65
C44 (GPa)	69	69.1	81

Table 2
Lattice constants and elastic constants for the BCT5 phase.

	Plane wave pseudopotential [13]	Stillinger–Weber [13]	Tersoff (this work)
a (Å)	3.32	3.3544	3.298
c (Å)	5.97	6.5148	6.468
E (eV/atom)	−4.41	−4.24	−4.419
C11 (GPa)	144	415	162
C12 (GPa)	124	243	108
C13 (GPa)	45	139	76
C33 (GPa)	160	208	205
C44 (GPa)	35	40	49
C66 (GPa)	63	101	143

Table 3
The lattice constants and elastic constants for the β-Sn phase of silicon.

	Tersoff [19]	Tersoff (this work)	Experimental [11]
a (Å)	4.905	4.903	4.686
c (Å)	2.57	2.568	2.585
E (eV/atom)	−4.3027	−4.3023	
C11 (GPa)		297	
C12 (GPa)		60	
C13 (GPa)		39	
C33 (GPa)		378	
C44 (GPa)		36	
C66 (GPa)		29	

It should be noted that this value is but a measure of how far the bonds around a given atom are from the perfect diamond cubic structure and elastic strain will affect the value. However, as phases will have particular bond orientations their ideal structures will have specific angular values. An atom that has an angular value similar to the ideal value for a given structure and the correct coordination number can then be said to have the bonding characteristic of that phase. While the angular value might not be unique to a given phase, i.e. diamond cubic and hexagonal diamond both read as 0, it is a useful asset in identifying regions that can be examined closer for phase confirmation or in obtaining an estimate of the amount of a given phase that is present.

When compressed along the [1 0 0] crystalline orientation at 0 K, the 5 and 10 nm spheres first behaved elastically, then yielded by disordering at the high stress regions near the contact areas. Cross sections of the 10 nm sphere are seen in Fig. 5a and b. Further compression resulted in the disordered region growing outward and surrounding the core. Small clusters of BCT5 were identified within the disordered regions. When the displacement was high enough that the disordered regions created by the top and bottom plates reached each other, the core region began transforming to β-Sn. The β-Sn core continued to grow up to unloading and remained after unloading. The final structure was seen to consist of three layers: a β-Sn core surrounded by a disordered region, which in turn was surrounded by elastically deformed DC.

Fig. 5c–e shows that for [1 0 0] compression at 300 K in the 10 nm sphere, a similar yielding behavior resulted with disordered regions leading to the formation of β-Sn in the core of the sphere at large displacements. However, there was a noticeable increase in the scatter of the atomic behavior throughout both the diamond cubic and β-Sn regions due to thermal fluctuations. Increasing the sphere size to 20 nm in diameter still resulted in regions of β-Sn, but the morphology differed by showing it initially forming close to one of the contact areas as opposed to the sphere's center.

Upon unloading, all of the [1 0 0] compressed spheres at 300 K exhibited extensive relaxation as the β-Sn began to revert to a four coordination structure, visible in Fig. 5e. To better characterize the relaxed region, a radial distribution function, RDF, was calculated for the atoms for the last recorded timestep of the 10 nm sphere (the same timestep shown in Fig. 5e). RDF was used as it has been shown to allow for a distinction between DC and the other relaxed silicon phases commonly referred to as Si-III (bc8) and Si-XII (r8) [17]. All three of these phases have a coordination number of 4 (using a cutoff distance of 3 Å) but can be distinguished from each other by having different next nearest neighbor distances which would show up as distinct peaks within the RDF. Fig. 6 shows the RDF for only the atoms with a coordination number of 4 revealing 2 broad peaks that correspond only to DC (2.35, and 3.84 Å) and no distinct peaks characteristic of either Si-III or Si-XII (3.2–3.45 Å). The broadness of the peaks suggests that at this timestep, the region is disordered/deformed classifying it as an amorphous phase that is close to the DC structure.

Interestingly, almost no β-Sn was seen resulting from compression in either the [1 1 0] or the [1 1 1] directions. Cross sections of these compressions in the 10 nm spheres are given in Fig. 7. Besides the lack of β-Sn, the most notable aspect of these results is the vast difference in behaviors at the two temperatures. For the [1 1 0] loading, the 0 K runs (Fig. 7a and b) showed large amounts of elastic strain prior to the amorphous yielding compared to the 300 K runs (Fig. 7c and d). In fact, the elastic strain for the [1 1 0] orientation at 0 K was high enough that the effective coordination number increased to 6 at the high stress regions prior to yield (Fig. 7a). However, the greatest difference in behavior due to changing temperatures is seen in the [1 1 1] compression tests. At 0 K, the high loads applied while the sphere is still elastic allows for the resulting yield to occur throughout the entire sphere as

Author's personal copy

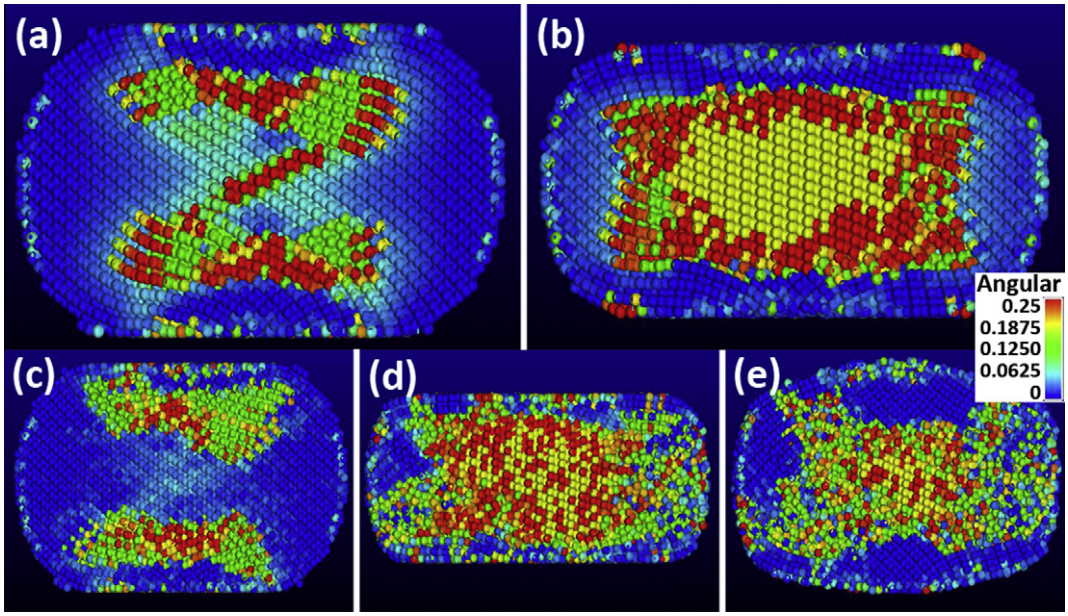

Fig. 5. Cross sectional images using the angular parameter to highlight the phase changes seen during [1 0 0] compression of 10 nm diameter spheres. (a) 0 K compression at 3.3 nm displacement resulting in green (mid grey) regions of BCT5. (b) 0 K after unloading showing a yellow (light grey) β-Sn core. (c) 300 K compression at 2.9 nm displacement. (d) 300 K compression at the maximum displacement (e) 300 K after unloading revealing that a large amount of the β-Sn had relaxed back to a 4 coordinated phase colored in blue (dark grey). (For interpretation of the references to colour in this figure legend, the reader is referred to the web version of this article.)

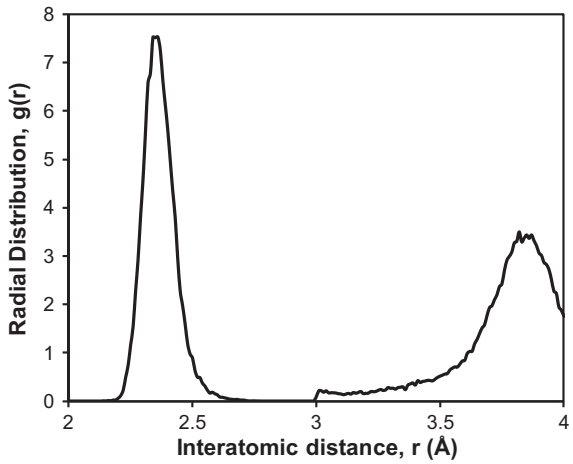

Fig. 6. Radial distribution function for the 4 coordinate relaxed phase of the final timestep of the 10 nm [1 0 0] compressed sphere at 300 K. Only peaks for DC at 2.35 and 3.84 Å are seen and no distinguishing peaks are seen between 3.2 and 3.45 Å that would indicate one of the other known relaxed silicon phases. The nearest neighbor cutoff value used to isolate the DC phase was 3 Å resulting in the sudden step at this value.

shown in Fig. 7e. At 300 K, yield occurs almost immediately upon contact and remains localized near the indenter–sphere interface leaving the center nearly undeformed shown in Fig. 7f.

The coordination number and the angular parameter values were also used to quantify the amounts of the different phases present. This was accomplished by counting the number of atoms with the correct coordination number for a particular phase along with an angular value within a range about the ideal value. For instance, β-Sn was taken to be atoms that had 6 nearest neighbors and an angular value between 0.17 and 0.25. Although this analysis produces a specific value, it should be considered as a rough estimate as it does not take long range order or elastic strain into account.

Results in Fig. 8 shows that for [1 0 0] compression, the β-Sn quickly increases in concentration at the higher strains and approaches nearly 10% at the maximum strain. During the initial unloading, the elastic strain is released from the sphere resulting in the measured β-Sn value increasing for a short period as strained β-Sn relaxes to its ideal configuration. Following this, the β-Sn in the 0 K simulation levels out whereas the 300 K simulation shows a marked decrease due to the reverse phase transformation. The values calculated for the [1 1 0] and [1 1 1] orientations show *only 1 and 2% respectively for the atoms reaching the criteria for β-Sn*, confirming the results of the visual analysis.

The concentrations of DC and BCT5, along with β-Sn as a function of strain are shown in Fig. 9 for the [1 0 0] compressed 10 nm sphere at 300 K. Prior to loading, only 90% of the atoms in the sphere register as DC. The 10% classified as other at this point is due to the surface atoms being excluded for not having 4 nearest neighbors. At a strain of 0.2, the fraction of DC is seen to begin to rapidly decrease, while a small amount of BCT5 begins to form. The first β-Sn forms soon after this, but appreciable amounts do not appear until roughly a strain of 0.3. The BCT5 concentration decreases slightly when β-Sn forms. After a strain of 0.4, β-Sn continues to increase steadily while both BCT5 and DC decrease. At the maximum strain, 45% of the material is not classified as being one of the three phases with β-Sn occupying roughly 9%, BCT5 roughly 13%, and DC roughly 33%. Upon unloading, an initial increase in all of the values is seen as the sphere elastically relaxes allowing more atoms to be counted as a particular phase. Further unloading shows the amount of DC increase and the amount of β-Sn decrease due to the reverse phase transformation.

Together, the results suggest a different explanation for the hardening behavior seen by Valentini et al. [2] for Si sphere compression modeled with the Tersoff potential. For all orientations, the 0 K compressions show that very large contact stresses are reached and the applied load is steadily increasing all the way up to unloading. In contrast, the 300 K compressions initially behave elastically, but then clearly yield with little hardening afterwards. Furthermore, the β-Sn transformation was seen during the [1 0 0] compression at both 0 K and 300 K, but was not present during

Author's personal copy

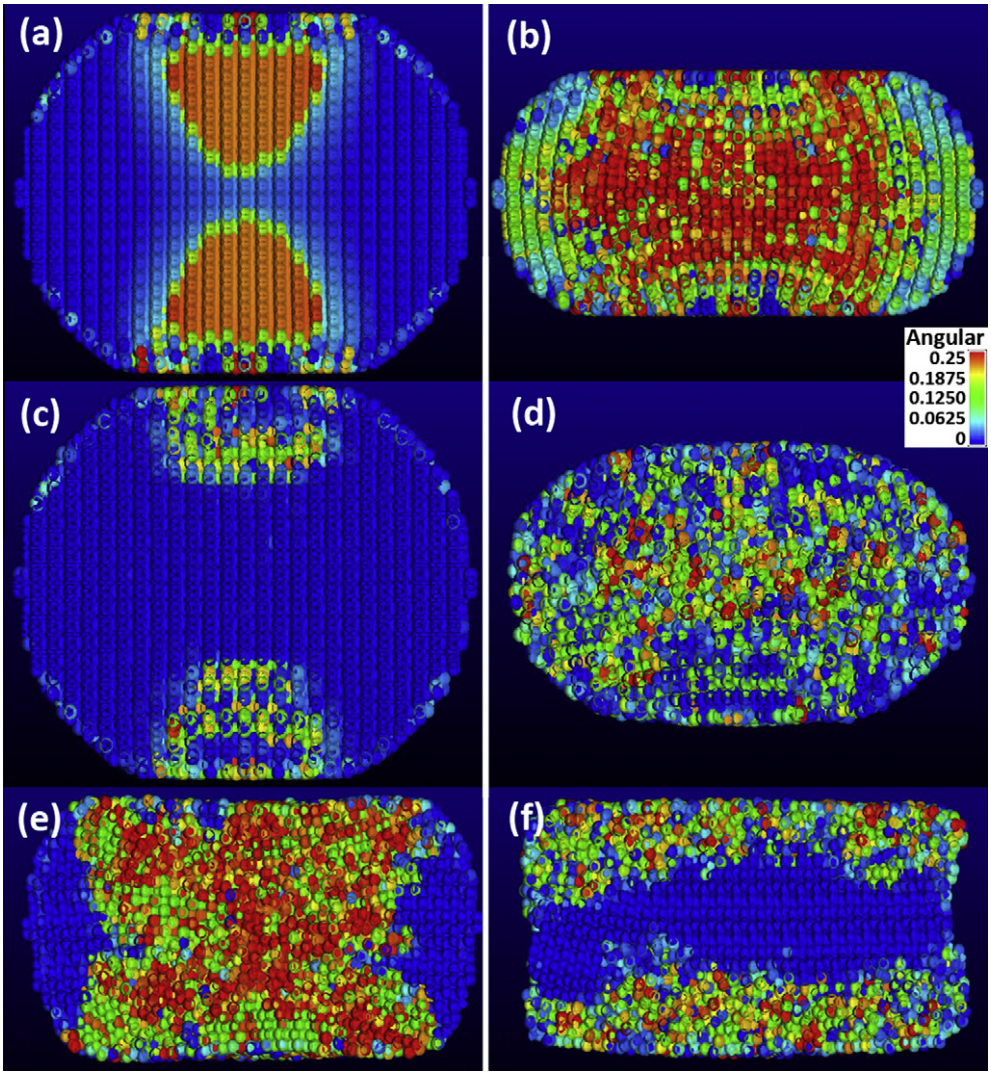

Fig. 7. Cross section images of 10 nm diameter spheres colored with angular values. (a) 2.5 nm displacement of [1 1 0] compressed sphere at 0 K resulting in regions of high elastic strain that appear different with the angular parameter due to the measured coordination increasing to 6. (b) Post compression of the [1 1 0] 0 K sphere with no distinguishable regions of a particular phase. (c) 1.7 nm displacement of [1 1 0] compressed sphere at 300 K showing that yield occurs much earlier than at 0 K preventing the extensive elastic behavior seen in (a). (d) Post compression of the [1 1 0] 300 K sphere also with no distinguishable regions of a particular phase. (e) Post compression of the [1 1 1] 0 K sphere showing disordered material throughout. (f) Post compression of the [1 1 1] 300 K sphere revealing disorder only at the surface near the contact areas.

compression for the other orientations. This suggests that the high contact stresses and hardening behavior are independent of the β-Sn phase transformation. Instead, it appears that these high contact stress values are due to the Tersoff potential having a high resistance to plastic yielding for 0 K simulations. Since yield stress generally scales with modulus, this would be consistent with the observations in Fig. 3 and of the unloading slopes at 0 K being greater than those at 300 K for all three orientations even when little β-Sn is present.

Even though the β-Sn transformation is widely accepted as occurring experimentally during indentation of flat silicon surfaces in different orientations [20–23], no direct evidence of the transformation, either as elbows in the unloading curve or the presence of other phases in a diffraction pattern, has been observed for small compressed silicon nanoparticles [1,24–26]. This was for spheres less than about 100 nm in diameter. The simulations presented here show that β-Sn will only form within the nanospheres when compressed along the [1 0 0] crystallographic direction. From the experimental results, the particles' orientations are unknown with respect to the compression direction and assumed to be random due to the fabrication technique [1,25]. Therefore, it follows that many of the nanoparticles will not undergo the β-Sn transformation as their orientation is not favorable. Conversely, if the orientation is the only decisive factor, it is possible that some of the particles would show evidence of the transformation.

As one representation of the β-Sn structure is as a tetrahedral compression of the DC structure along one of the <1 0 0> directions, it makes sense that [1 0 0] compressions result in the formation of this phase. However, for the other orientations, the behavior is different within the compressed spheres than it is for indented bulk silicon suggesting that the spherical geometry is less favorable to the formation of β-Sn. The most notable difference between the two geometries is that the sphere is much less constrained in the directions normal to the applied load than an indented flat surface is. This allows for the sphere to easily expand in these directions, as seen with the contact area analysis. Because of this the hydrostatic pressure within the spheres will be less for a given loading than bulk indentation potentially making the β-Sn transformation less likely. As this is a qualitative assessment, future work would be necessary to determine exactly how these stress states differ.

Author's personal copy

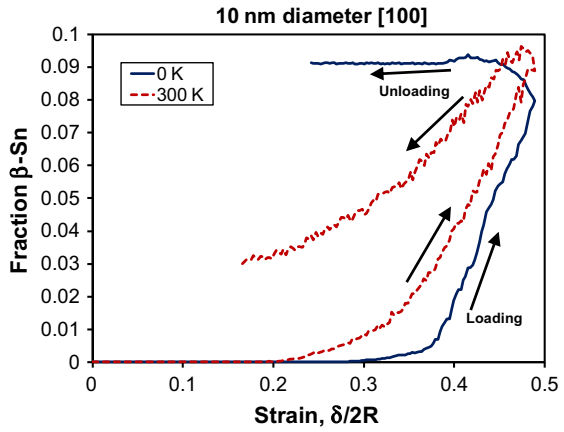

Fig. 8. Fraction of β-Sn plotted vs. strain for the 10 nm diameter [1 0 0] compressed spheres.

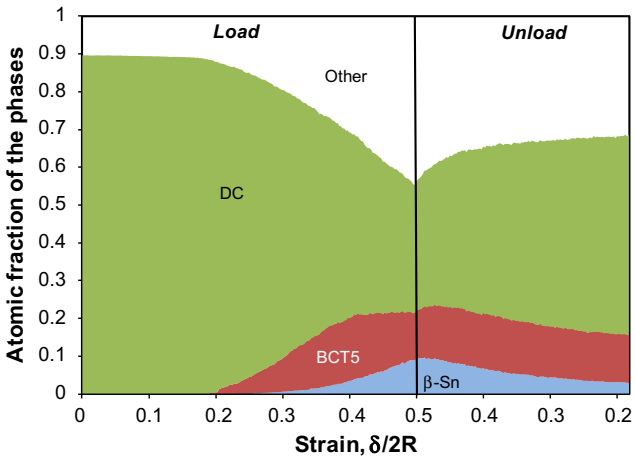

Fig. 9. The progression of the estimated fractions of the different phases as seen within the 10 nm diameter [1 0 0] compressed sphere at 300 K. The solid vertical line marks the maximum displacement, after which the sphere is unloaded.

It should also be noted that there are considerable differences between the simulation and experimental conditions. The largest simulations presented here are half the size of the smallest particles that have been experimentally compressed. In addition, the rate of compression is quite different: Nowak et al. reported an experimental displacement rate of 10 nm s^{-1} resulting in compression runs around 10 s [26], whereas the displacement rate of 6.25×108 nm s^{-1} for the simulations resulted in total compression runs lasting around 10–20 ns. Either of these factors could greatly influence the mechanical response and make different yielding mechanisms more favorable.

3.2. Dislocations

In addition to the phase transformations, dislocation yielding was also observed in three of the simulations: 5 nm 600 K [1 0 0] and [1 1 0] compressions and 20 nm 300 K [1 0 0] compression.

Distinguishing dislocations within the 5 nm 600 K simulations was difficult due to the small number of atoms and the high thermal scatter. However, hints of dislocation motion were observed by plotting the direction of the slip vectors of the atoms. By restricting the plot to only showing atoms with slip vector magnitudes around what is expected for perfect dislocations, small planar regions were seen to contain parallel slip vectors. As the slip vector indicates the region where a dislocation with a particular Burgers vector equal to the slip vector has passed through, finding a planar region where all of the atoms have nearly identical slip vectors indicates that a dislocation, however short lived, had existed there. Both of the [1 0 0] and [1 1 0] compressions contained one of these dislocation hints, with the [1 0 0] shown in Fig. 10. Since no dislocations were observed in the 5 and 10 nm spheres at 0 K and 300 K, a clear temperature dependence on dislocation nucleation is evident at this size scale.

For the 20 nm diameter 300 K simulation, a total of nine dislocations were observed prior to unloading. The first of these dislocations is shown in Fig. 11. The presence of these dislocations indicates that there is a cutoff size for dislocation formation between 10 and 20 nm diameters at 300 K. Close analysis of these dislocations revealed them to be perfect 1/2<1 1 0> shuffle set dislocations. They were seen to form at high strains when there was already substantial regions that had deformed to an intermediate state between the DC and β-Sn phases. Slipped planes indicating the motion of these dislocations appeared at the edge of the disordered regions going to the surface of the sphere.

The fact that dislocations can be observed in these MD simulations of silicon nanospheres allows for a comparison with the hardening theory proposed in the experimental papers. In short, this theory states that the high hardness values are the result of the buildup of dislocations confined within the small particle dimensions. Due to the presence of an oxide layer on the surface of the sphere, any dislocations that form within the sphere are delayed from terminating on a free surface leading to dislocation pileups. These pileups potentially result in a back stress opposing the applied load resulting in high hardness values. As the particle size decreases, the volume that the dislocations are confined within also decreases allowing for higher stresses to be reached [26]. It is also believed that this behavior will have a lower limit when the particle passes a critical size that is necessary for dislocations to form [1].

Only the 20 nm diameter sphere compressed at 300 K showed multiple dislocations, confirming that there is a critical size for dislocation nucleation. However, no accompanying hardening behavior occurred as the dislocations all formed individually and quickly disappeared upon reaching the surface as no oxide barrier was present. There was never more than one dislocation present within the sphere at any timestep thus no dislocation interactions or pileups.

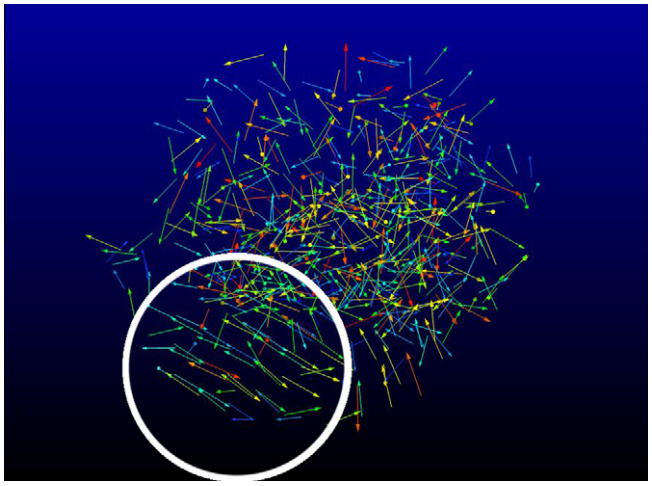

Fig. 10. Image of the slip vector direction for atoms with slip magnitudes close to a perfect dislocation within the [1 0 0] compressed 5 nm diameter sphere at 600 K. The circle indicates a planar region where the slip vectors are oriented nearly parallel to each other indicating the presence of a dislocation.

Author's personal copy

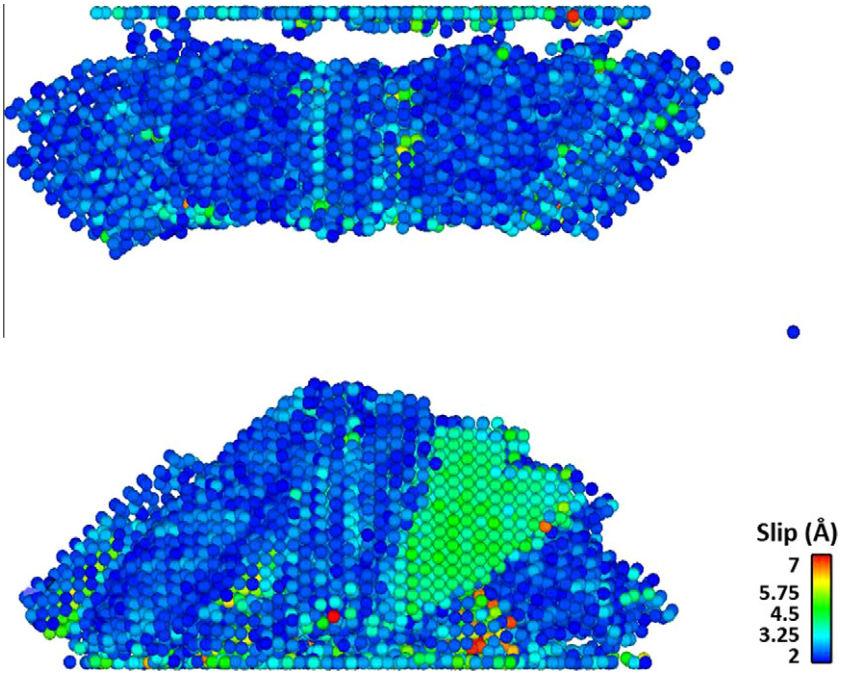

Fig. 11. Atoms colored with the slip vector magnitude for [1 0 0] compression of a 20 nm diameter sphere at 300 K. The blue (dark) regions of low slip (2–3 Å) has a volume type shape representing phase change-type deformation resulting in regions of BCT5 and β-Sn. The green (light) region shows a plane that has slipped due to a full 1/2<1 1 0>{1–11} dislocation. (For interpretation of the references to colour in this figure legend, the reader is referred to the web version of this article.)

Witnessing dislocation hardening and interactions using molecular dynamics would require that multiple dislocations be present within the sphere at the same time. To obtain this, dislocations must form more readily and/or must be impeded from reaching and disappearing at the sphere's surface. The former could be possible by changing the atomic potential used to one that is more prone to dislocation behavior, while the latter can be accomplished by introducing a surface barrier representative of the oxide layer. Also, increasing the sphere size would accomplish both of these conditions as only the largest sphere showed dislocation behavior and further increases in size would mean that any dislocations that formed would have to travel further to reach the surface. Incorporating an oxide layer and increasing the sphere size would make the simulations more comparable to the experimental results, but doing either would require an increase in the complexity and computational time. Changing the potential could result in an overall simulated behavior that is less realistic than what is presented here, but if it is capable of showing multiple concurrent dislocations in sizes comparable to those here, it would offer a simple and efficient way of studying the dislocation interactions. Further work is currently being done investigating all of these possibilities.

4. Conclusions

The yielding properties observed within Tersoff modeled silicon nanospheres showed a high dependence on changes in temperature, orientation and sphere size. For three temperatures and three orientations, β-Sn is only seen to appear in substantial amounts during [1 0 0] compression. Only the simulations near 0 K show high contact stress values indicating that the chosen atomic potential fails to accurately model the experimental hardening at ambient temperatures. As the β-Sn transformation observed in these simulations forms only for specific compression orientations and is independent of the hardness behavior seen, it is highly unlikely for the β-Sn to play a role in the experimentally observed hardening. The observed large contact stress values at 0 K are thus attributed to a high yielding point, resulting in elastic behavior at large strains and a stiffening behavior. Dislocation behavior is also identified and indicates that a critical size and temperature must be exceeded for dislocations to nucleate. Although no hardening results from the dislocations in these simulations, it is proposed that the larger dimensions and the presence of an oxide on the experimentally observed particles would result in a greater number of dislocations to be present within the particle potentially allowing for dislocation hardening.

Acknowledgements

This work was partially supported in part (RB and LMH) by the National Science Foundation Grant NSF_CMMI 0800896. One of us (WWG) would like to acknowledge additional support of the Air Force through an AOARD-08-4131 program dedicated to understanding plasticity and fracture in hard materials and the Abu Dhabi-Minnesota Institute for Research Excellence (ADMIRE); a partnership between the Petroleum Institute (PI) of Abu Dhabi and the Department of Chemical Engineering and Materials Science of the University of Minnesota. Additionally, four of us (LMH, XZ, JAZ, and NMR) were supported by Sandia, Livermore. Sandia is a multi-program laboratory operated by Sandia Corporation, a Lockheed Martin Company, for the United States Department of Energy's National Nuclear Security Administration under contract DEAC04-94AL85000.

References

[1] W.W. Gerberich, W.M. Mook, C.R. Perrey, C.B. Carter, M.I. Baskes, R. Mukherjee, A. Gidwani, J. Heberlein, P.H. McMurry, S.L. Girshick, J. Mech. Phys. Sol. 51 (2003) 979.
[2] P. Valentini, W.W. Gerberich, T. Dumitrica, Phys. Rev. Lett. 99 (2007) 175701.
[3] J. Tersoff, Phys. Rev. B 37 (1988) 6991.
[4] LAMMPS Molecular Dynamics Simulator. <http://lammps.sandia.gov/>.
[5] W.G. Hoover, Phys. Rev. A 31 (1985) 1695.
[6] J. Tersoff, Phys. Rev. B 38 (1988) 9902.
[7] F.H. Stillinger, T.A. Weber, Phys. Rev. B 31 (1985) 5262.

Author's personal copy

[8] J.A. Zimmerman, C.L. Kelchner, P.A. Klein, J.C. Hamilton, S.M. Foiles, Phys. Rev. Lett. 87 (2001) 165507.
[9] M. Vergeles, A. Maritan, J. Koplik, J.R. Banavar, Phys. Rev. E 56 (1997) 2626.
[10] K.L. Johnson, Contact Mechanics, Cambridge University Press, Cambridge, MA, 1985.
[11] J.C. Jamieson, Science 139 (1963) 762.
[12] M.I. McMahon, R.J. Nelmes, Phys. Rev. B 47 (1993) 8337.
[13] L.L. Boyer, E. Kaxiras, J.L. Feldman, J.Q. Broughton, M.J. Mehl, Phys. Rev. Lett. 67 (1991) 715.
[14] C.F. Sanz-Navarro, S.D. Kenny, R. Smith, Nanotechnology 15 (2004) 692.
[15] D.E. Kim, S.I. Oh, Nanotechnology 17 (2006) 2259.
[16] Y.H. Lin, T.C. Chen, Appl. Phys. A 92 (2008) 571.
[17] Y.H. Lin, S.R. Jian, Y.S. Lai, P.F. Yang, Nanoscale Res. Lett. 3 (2008) 71.
[18] D.E. Kim, S.I. Oh, J. Appl. Phys. 104 (2008) 013502.
[19] H. Balamane, T. Halicioglu, W.A. Tiller, Phys. Rev. B 46 (1992) 2250.
[20] A.B. Mann, D. van Heerden, J.B. Pethica, T.P. Weihs, J. Mater. Res. 15 (2000) 1754.
[21] V. Domnich, Y. Gogotsi, S. Dub, Appl. Phys. Lett. 76 (2000) 2214.
[22] T. Juliano, V. Domnich, Y. Gogotsi, J. Mater. Res. 19 (2004) 3099.
[23] J. Jang, M.J. Lance, S. Wen, T.Y. Tsui, G.M. Pharr, Acta Mater. 53 (2005) 1759.
[24] W.W. Gerberich, W.M. Mook, M.J. Cordill, C.B. Carter, C.R. Perrey, J.V. Heberlein, S.L. Girshick, Int. J. Plast. 21 (2005) 2391.
[25] J. Deneen, W.M. Mook, A. Minor, W.W. Gerberich, C.B. Carter, J. Mater. Sci. 41 (2006) 4477.
[26] J.D. Nowak, A.R. Beaber, O. Ugurlu, S.L. Girchick, W.W. Gerberich, Scr. Mater. 62 (2010) 819.